Functional Perovskites – From Epitaxial Films to Nanostructured Arrays**

By *Ionela Vrejoiu, Marin Alexe, Dietrich Hesse,* * and *Ulrich Gösele*

Functional perovskite materials gain increasing significance due to their wide spectrum of attractive properties, including ferroelectric, ferromagnetic, conducting and multiferroic properties. Due to the developments of recent years, materials of this type can conveniently be grown, mainly by pulsed laser deposition, in the form of epitaxial films, multilayers, superlattices, and well-ordered arrays of nanoislands. These structures allow for investigations of preparation–microstructure–property relations. A wide variation of the properties is possible, determined by strain, composition, defect contents, dimensional effects, and crystallographic orientation. An overview of our corresponding work of recent years is given, particularly focusing on epitaxial films, superlattices and nanoisland arrays of (anti)ferroelectric and multiferroic functional perovskites.

1. Introduction

Perovskite and layered-perovskite oxides are complex materials with a wide spectrum of attractive properties, as they can be insulating dielectrics, metals, ferro-/antiferro-electrics, ferro-/antiferromagnets,[1] multiferroics,[2] superconductors,[3] or thermoelectrics,[4] and thus exhibit a large variety of functional behavior. Perovskites are cubic or pseudocubic ABO_3-type of materials earning their name from the prototype $CaTiO_3$ mineral called perovskite, after the Russian mineralogist L. A. Perovski (1792–1856).

In addition to proper perovskite materials, layered perovskites, such as the high temperature superconductors $YBa_2Cu_3O_7$ (YBCO) and $Bi_2Ca_2SrCu_2O_8$, or the ferroelectric La-substituted $Bi_4Ti_3O_{12}$ (BLT) and $SrBi_2Ta_2O_9$, are very attractive materials as well. Because of their highly anisotropic crystal structure, epitaxial thin films of the latter materials can easily be grown with the [001] axis perpendicular to the film plane (i.e., in the so-called *c*-axis orientation). However, nearly purely *a*-axis oriented epitaxial YBCO films could be grown on $SrTiO_3$ (100) and $LaAlO_3$ (100) by high-pressure single target 90° off-axis sputtering, making the fabrication of sandwich-type Josephson junctions possible.[5] Ferroelectric *c*-axis oriented $Bi_4Ti_3O_{12}$ films have a negligible polarization component along the film normal, because the vector of the (major) spontaneous polarization in these layered perovskite materials is along the *a* axis. Lee et al. made the breakthrough succeeding to grow epitaxially twinned, uniformly *a*-axis oriented BLT thin films on yttria-stabilized zirconia-buffered Si(100) by pulsed laser deposition, using kinetic growth conditions of high deposition rate and high oxygen pressure.[6] Although layered perovskite materials are most interesting and relevant, in this paper we will mostly limit ourselves to reviewing materials that have the proper perovskite structure.

Nowadays the quality of the heteroepitaxial perovskite films and superlattices grown on closely matched single crystal substrates achieved a degree of perfection similar to the heteroepitaxy of semiconductors, especially due to the advances in the in situ control of the layer-by-layer deposition in molecular beam epitaxy (MBE) and reflection high energy electron diffraction (RHEED)-assisted pulsed laser deposition. More exquisite systems such as laser MBE attached to a synchrotron beam line have been developed for probing the electronic structure of surfaces and interfaces as the heterostructure is being grown.[2] The high structural quality of the currently grown epitaxial perovskite films permits the study of important physical properties, as the extrinsic and frequently predominant contribution of structural defects has been greatly reduced. Furthermore, using the combination of perovskites with different physical properties in

[*] Prof. D. Hesse, Dr. I. Vrejoiu, Dr. M. Alexe, Prof. U. Gösele
Max Planck Institute of Microstructure Physics
Weinberg 2, 06120 Halle (Germany)
E-mail: hesse@mpi-halle.de

© 2008 WILEY-VCH Verlag GmbH & Co. KGaA, Weinheim

epitaxial heterostructures, e.g., combining ferroelectric with ferromagnetic perovskites, new functionalities can be engineered. For instance, magnetoelectric coupling in ferromagnetic/ferroelectric structures is extremely appealing for device fabrication, if it allows the switching of the magnetization on applying an electric field rather than a current, mimicking the electric-write process in ferroelectric random access memories.

The present article focusses on the work of our group in recent years, mainly presenting examples for growth and microstructure of the grown perovskite films, superlattices, and nanostructures. For more information on the physical properties of these structures, e.g., polarization–voltage curves, switching properties, etc., which mostly have been studied as well, the reader is referrred to the cited original work.

2. Epitaxial Ferroelectric Films

2.1. Structural Defects in Epitaxial Ferroelectric Films

In most materials, structural defects can play detrimental roles, drastically affecting the physical properties of the materials and limiting their performance when integrated into devices. In the case of ferroelectrics, the effects of misfit and threading dislocations (MDs and TDs, respectively) have been investigated on nanostructures and epitaxial films. The strain field surrounding dislocations is predicted to dramatically disturb the ferroelectric and dielectric properties of the surrounding material.[7–9] In nanostructures, due to their confined dimensions, the influence of defects is even more pronounced, because of the enhanced relative volume of the defective regions. Chu et al.[10] performed a study of quantitative high-resolution electron microscopy and piezoresponse force microscopy (PFM) on epitaxial $PbZr_{0.52}Ti_{0.48}O_3$ nanoislands (see also Sec. 5.1.). We demonstrated that these nanoislands exhibited edge-type misfit dislocations, the strain fields of which were perturbing relatively large tubular regions of PZT with a cross-section of 4 nm (height) times 8 nm (width).[10] Therefore, PZT islands that were ca. 10 nm high showed an apparent polarization instability, associated with the distorted PZT lattice within the strain fields. The PZT lattice deviated from the expected tetragonal structure and the long-range correlations of local polarizations thus broke down, resulting in polarization instability.

Although it is intuitively accepted that MDs and TDs have an important impact in the case of epitaxial thin films, too, it is quite difficult to make the quantitative correlation between the presence of various types of dislocations and the effective ferroelectric and dielectric properties of the material.[9,11–14] Nagarajan et al. reported a quantitative study of the thickness dependence of the polarization and piezoelectric properties of epitaxial PZT films with two compositions, $PbZr_{0.52}Ti_{0.48}O_3$ (PZT52/48) and $PbZr_{0.2}Ti_{0.8}O_3$ (PZT20/80), grown on $SrRuO_3$-coated (001) $SrTiO_3$ [8] Cross-section TEM microscopy images of 20 nm thin PZT films of both compositions showed that dislocations were present in the PZT films. However MDs formed in a much higher density for the PZT 52/

Dietrich Hesse is head of the Nanoengineering of Functional Oxides group at Max Planck Institute of Microstructure Physics, Halle, Germany, and Adjunct Professor of Experimental Physics at Martin Luther University Halle-Wittenberg, Germany. He received his Physics Diploma from Moscow State University (Russia, 1973) and his Ph.D. from Martin Luther University Halle-Wittenberg (1985). He is a recipient of the Leibniz Silver Medal Award of the German Academy of Sciences "for achievements in studies of solid state reactions" (1989). From 1992 to 1998 he was member of the Coordinated Research Project "Solids far from equilibrium" at Georg August University Göttingen, Germany. In 1998 he habilitated at Martin Luther University, and in 2006 was appointed Adjunct Professor. From 2001 to 2007 he was member of the Scientific Council of the Max Planck Society. His research interests include ferroelectric and multiferroic nanostructures, but also solid state reactions on the nanometer scale including, e.g., the formation of compound nanotubes and nanowires by solid state reactions.

Ionela Vrejoiu has worked as a postdoc associate in the group of Nanoengineering of Functional Oxides at Max Planck Institute of Microstructure Physics, Halle, Germany since 2005. She was born in Bucharest, Romania. She received her M. Sc. from University of Bucharest (Physics Department) in 2000 and her Ph. D. from Johannes Kepler University (Institute of Applied Physics), Linz, Austria, in 2004. At MPI Halle her research has been dedicated to epitaxial thin films and superlattices of perovskites with various physical properties, e.g. ferroelectric $Pb(Zr,Ti)O_3$, ferromagnetic $La(Sr,Mn)O_3$ and $SrRuO_3$, multiferroic $BiFeO_3$, fabricated by pulsed laser deposition.

48 film, which has a larger in-plane lattice mismatch with the $SrTiO_3$ substrate (-3.9% for PZT 52/48, but only about -0.7% for PZT 20/80, at growth temperature). As a consequence, a drastic decrease of both the switchable polarization ΔP and piezoelectric coefficient d_{33} was observed for PZT 52/48 films thinner than 100 nm. The lattice-matched PZT 20/80 films, with low density of dislocations, showed no scaling in ΔP or d_{33} down to 15 nm. The severe drop in ΔP and d_{33} values in the PZT 52/48 systems occurring for much thicker layers indicated the significant role of dislocations in the size effects in ferroelectric thin films and nanostructures.

2.2. "Defect-Free" Epitaxial Ferroelectric Films

In the frame of the above considerations, Vrejoiu et al. reported on the fabrication of single crystalline $PbZr_{0.2}Ti_{0.8}O_3$ thin films grown on $SrRuO_3$-coated vicinal $SrTiO_3$ (STO) (100) substrates, pursuing the growth of ferroelectric epitaxial films free from extended structural defects.[15] The films were fabricated by pulsed laser deposition (PLD). The quality of the vicinal STO substrates (CrysTec, Berlin) and their prior treatment by etching in buffered hydrofluoric acid and annealing at 1000–1100 °C proved to be critical. The employment of TiO_2-terminated single unit cell-stepped STO(100) surfaces was a prerequisite for achieving the step flow growth regime for the oxide electrode, $SrRuO_3$ (SRO).[16] Step flow growth renders the SRO layer pseudomorphic and in-plane coherent to the STO(100) substrate. Furthermore, step flow grown SRO serves as a template for the subsequent layer-by-layer growth of the $PbZr_{0.2}Ti_{0.8}O_3$ (PZT20/80) epitaxial films, which occurs under carefully optimized PLD conditions. The particular composition PZT20/80 was chosen because it is nominally tetragonal at room temperature, and c-axis grown films would also have relatively low in-plane lattice mismatch on SRO/STO (100).

Figure 1 summarizes the results of structural and ferroelectric characterization of our PZT20/80 films. Figure 1a and b show high resolution TEM (HRTEM) and TEM cross section micrographs taken on PZT20/80/SRO/STO (100) heterostructures grown under optimized PLD parameters. For comparison, Figure 1c displays the cross section TEM micrograph of a 250 nm thick PZT20/80 film grown under non optimized conditions. In this PZT20/80 film a high density of extended structural defects such as TDs and stacking faults (SFs) were found by TEM and HRTEM and were correlated with the microscopic studies of the backswitching of the polarization observed by piezoresponse force microscopy (PFM).[14] Further evidence of the detrimental role played by these defects on the ferroelectric properties of the PZT films is given by the macroscopic polarization measurements performed through large top Pt/SRO electrodes (electrode area ≤ 0.09 mm^2). Figure 1d and e show the polarization hysteresis and the switching current loops measured on a PZT20/80 film free from TDs and SFs and on a PZT20/80 film with high density of such defects,[14] respectively. The remnant polarization is considerably higher for the high structural quality film,
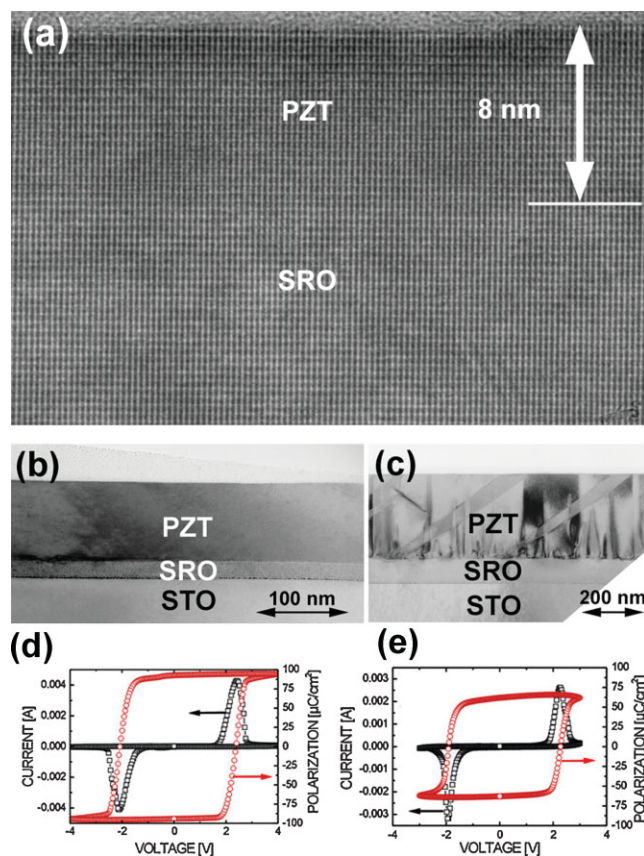

Figure 1. Microstructure and properties of epitaxial PZT20/80 films: a) cross section HRTEM micrograph of an 8 nm PZT20/80 film coherently grown on SRO/STO(100); cross section TEM micrographs of b) a "defect-free" 90 nm thin PZT20/80 film and c) a defective 250 nm thin PZT20/80 film; switching current and polarization hysteresis curves measured at 1 kHz and room temperature on d) a "defect-free" and e) a defective PZT20/80 film. (After Refs. [14, 15]).

$P_r = 95 \, \mu C \, cm^{-2}$, whereas the defective film has around $P_r = 65 \, \mu C \, cm^{-2}$.

The high structural quality of the optimized PZT20/80 films of Vrejoiu et al. also allowed detailed studies of the extrinsic contributions to the apparent thickness dependence of the dielectric constant[17] and of the origin of leakage currents[18] in epitaxial PZT20/80 films.

There are also other reports on PZT20/80/SRO/STO (100) heterostructures grown by PLD as well.[19,20] Lee et al. reported, with first principles atomistic PZT models as theoretical support for the experimental data, that the remnant polarization of their strained PZT20/80 films cannot be higher than $\sim 93 \, \mu C \, cm^{-2}$, despite the fact that they have a large tetragonality, $c/a \cong 1.09$, compared to bulk PZT20/80 that has $c/a \cong 1.05$. Some structural differences do exist between the films of Lee et al. and those grown by Vrejoiu et al.,[15] as can be seen from the TEM micrographs in Figure 1c and d of Lee's paper,[20] where it is shown that the 15 nm PZT20/80 films already have misfit dislocations and 116 nm thin films have a large density of threading dislocations, complete strain relaxation occurring for films thicker than 40 nm. For Lee's

PZT20/80 films the measured remnant polarization was almost tetragonality-independent, $P_r = 82\,\mu C\ cm^{-2}$. Despite the similarities, the strained PZT20/80 films of Vrejoiu et al. have less dislocations and retain partially the strain up to thicknesses of 90 nm (Fig. 1a and b), which should be the result of optimized growth and cooling conditions.[15]

Lee et al. argued that in highly polar ferroelectrics, such as PbTiO$_3$ and PZT, the polarization is almost independent on the compressive biaxial epitaxial strain.[20] This is in contrast to the case of strained BaTiO$_3$ epitaxial films for which pronounced enhancement of the polarization was observed,[21] as a result of the less polar nature of BaTiO$_3$ that makes it more sensitive to strain.

2.3. Domains in Epitaxial Ferroelectric Films

Another important aspect regarding ferroelectric (ultra)thin films are the ferroelectric domains. Ferroelectric domains are of great interest, as they may determine the switching properties of the films and can even be used for information storage.[22] At room temperature, tetragonal *c*-axis grown epitaxial PZT films exhibit a large variety of domain patterns, depending upon growth conditions, substrate employed and boundary conditions (open or short circuit). The 90° *a–c* ferroelectric/ferroelastic domains formed in ferroelectric heteroepitaxial tetragonal films have been studied both theoretically and experimentally in great detail.[23] Similarly to the formation of misfit dislocations in heteroepitaxial strained films, Pompe et al.[23] investigated the twin formation as a mechanism for strain energy release and introduced a critical thickness for twin domain formation in heteroepitaxial tetragonal films. They predicted that in certain moderate strain conditions a critical film thickness exists, below which the film would stabilize as a uniformly *c*-oriented film. For our heteroepitaxial tetragonal PZT20/80 films grown on SRO/ STO (100) this critical thickness is larger than 90 nm, as seen from TEM (see Fig. 1b) and PFM, and it depends very strongly on the growth conditions.[15] Our thicker (>100–150 nm) PZT20/80 films show *c–a–c* domain patterns as predicted by Pompe et al.[23] The *a*-domains were proven to be highly mobile under the influence of a non-uniform electric field and their movement was monitored by PFM.[24] Moreover, the movement of the minority *a*-domains in the matrix of *c*-domains was demonstrated to extrinsically enhance the dielectric permittivity and the piezoelectric response of the films.[24,25] Figure 2 shows the PFM piezoresponse images (1 μm × 1 μm) acquired on the free surface of a 150 nm thick, *c*-oriented PZT20/80 film that has *a*-domains. On the same 1 μm^2 area the modification of the *a*-domain pattern was monitored as a function of the applied dc bias voltages (Fig. 2a–d), and a significant change in the *a*-domain structure was observed, leading to the conclusion that the *a*-domains are mobile under the influence of a non-uniform electric field. The effect of the domain motion on the piezoelectric hysteresis loops measured by PFM is depicted by the schematic and the hysteresis loops shown in Figure 2e. Previous reports, such as
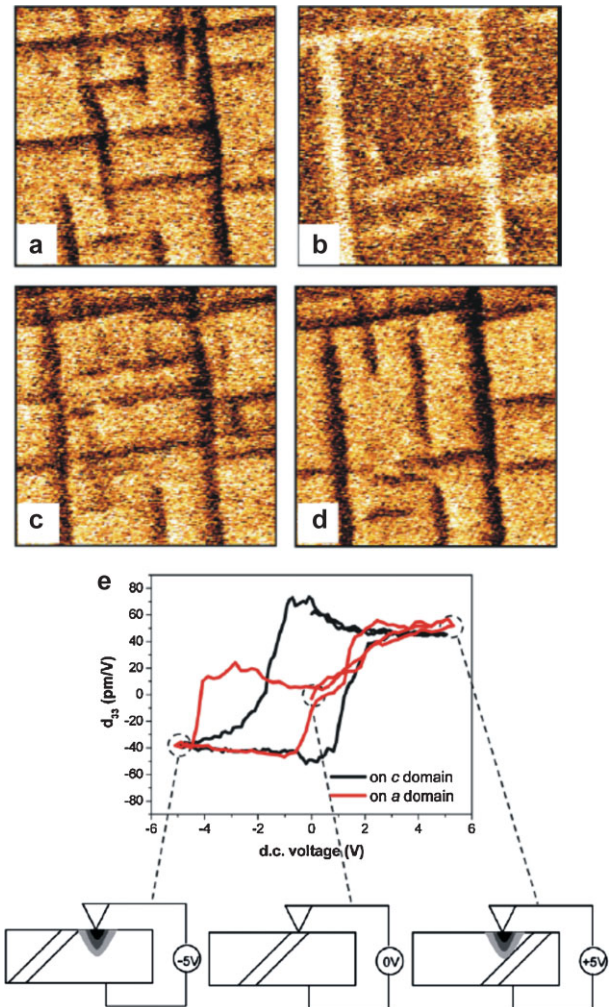

Figure 2. Out-of-plane piezo-response images (of the same $1 \times 1\,\mu m^2$ area) taken by PFM on the surface of a 150 nm thick PZT20/80 film with *c-a-c* twin domains, as a function of applied dc bias voltages: a) as-grown state; b) after −6 V dc, c) after +3 V dc, and d) after +6 V dc. In e) the effect of the motion of an *a*-domain on the acquired piezoelectric hysteresis loops is schematically shown (After Ref. [24]).

the one by Nagarajan et al., had shown that in a *c*-axis oriented PZT20/80 film the 90° *a*-domains became mobile only after patterning the thin film into micrometer-size islands, in order to reduce the clamping effects of the substrate.[26] A great enhancement of the piezoelectric coefficients resulted from the island patterning and was associated with the increased mobility of *a*-domains.

Further importance of the 90° twin domain walls in ferroelectric tetragonal epitaxial films was emphasized by a joint study of switching spectroscopy PFM and phase-field modeling on the nucleation centers for polarization switching.[27] The *a–c* domain wall junctions were found to have a lower nucleation potential for the polarization switching, compared with the surrounding *c*-domain matrix, and thus are preferential sites for the nucleation of polarization switching.

Outstanding progress in the study of 180° ferroelectric domains exhibited by thin films has been made recently by the
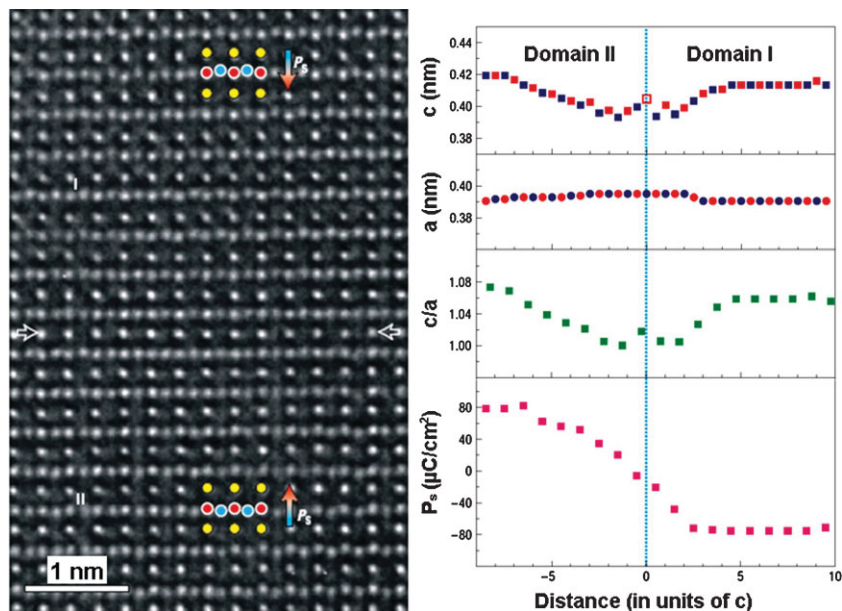
Figure 3. (Left) HRTEM image of a head-head coupled 180° domain wall segment inside a ~10 nm epitaxial PZT20/80 film with the horizontal arrows indicating the geometric central plane of the wall that is referred to as the origin for quantitative analysis of the dipole distortion across the wall area, which is summarized in the graphs shown on the right. P_S is the spontaneous polarization and a and c are the lattice parameters of PZT20/80. (After Ref. [28])

atomic-scale investigations of the electric dipoles in the vicinity of charged and uncharged domain walls (DWs).[28] By employing the novel negative spherical-aberration imaging technique, Jia et al.[28] explored the cation-oxygen dipoles near 180° head-to-head and head-to-tail coupled DWs in PZT20/80 films coherently sandwiched between $SrTiO_3$ films. The local tetragonality c/a and spontaneous polarization P_S inside the domains and across the DW could be calculated as well, the results being summarized in Figure 3, where a head-to-head coupled DW is shown and the c/a and P_S inside the two domains separated by this DW were derived. The wall thickness was estimated to 4 nm.

3. Multilayers and Superlattices with Epitaxial Ferroelectric Layers

Important advances have been made in the epitaxy of perovskite oxides either by molecular beam epitaxy or pulsed laser deposition. Therefore, in the last decade, multilayers (MLs) and superlattices (SLs) combining perovskites with various physical properties have emerged as extremely attractive artificially designed materials, exhibiting a broad range of interface- and strain-mediated phenomena.[29–31] Lee et al.[29] reported on tri-component asymmetric $BaTiO_3$/$SrTiO_3$/$CaTiO_3$ SLs on $SrRuO_3$-coated $SrTiO_3$(100). Two of the employed components, $SrTiO_3$ and $CaTiO_3$, are not ferroelectric in *bulk* form, at room temperature. Nevertheless, the $BaTiO_3$/$SrTiO_3$/$CaTiO_3$ SLs, as a result of epitaxial strain and interfacial effects, are ferroelectric and have an overall

50% enhancement of the global polarization of the SL with respect to a pure $BaTiO_3$ film grown in similar conditions as the SL.

3.1. Ferroelectric-Ferroelectric Superlattices

SLs of $[PbZr_xTi_{1-x}O_3/PbZr_yTi_{1-y}O_3]$, where $(x + y)/2 \cong 0.5$, have been investigated both theoretically and experimentally due to their envisaged very large enhancement of the electromechanical response compared with single phase thin films. Such SLs may in a two dimensional fashion "simulate" the composition of the morphotropic phase boundary of $PbZr_xTi_{1-x}O_3$ for $x \cong 0.5$. A peculiar case of epitaxial MLs consisting of ultrathin layers of two alternating $PbZr_xTi_{1-x}O_3$ compositions, namely PZT40/60 (nominally tetragonal) and PZT60/40 (nominally rhombohedral, as bulk, at room temperature) was investigated by Vrejoiu et al.[32] The PZT40/60/PZT60/40 MLs were grown on $SrRuO_3$-coated vicinal $SrTiO_3$(100) substrates by PLD. Significant structural transformations were observed by HR(TEM), XRD, and PFM in MLs with an individual layer thickness below ca. 8 nm. MLs of PZT40/60 (5 nm thin)/PZT60/40 (3 nm thin), with 44 such layers, had a uniformly tetragonal structure and exhibited characteristic uniformly tetragonal 90° a–c domain patterns, indicating that the nominally rhombohedral PZT60/40 layers adopted a tetragonal structure. The remnant polarization P_r of the 44-layer ML was larger than the P_r of a 16-layer ML which had 8 nm thin individual layers, all of which retained their rhombohedral and tetragonal structure, respectively. Figure 4 shows TEM cross section micrographs of two PZT40/60/PZT60/40 MLs, one with 4 layers (each of ca. 30 nm) (Fig. 4a) and the other with 30 layers (each of ca. 3 nm) layers (Fig. 4b). The cross section of the 4-layer sample showed that 90° twins formed only in the first and third layers, counting from the SRO electrode, which were of tetragonal PZT40/60, whereas the second and fourth layers, that were of PZT60/40 did not form 90° twins (Fig. 4a). This indicates that the 30 nm layers of PZT40/60 and PZT60/40 of this ML retained their tetragonal and rhombohedral structure, respectively. However, when both the PZT40/60 and PZT60/40 layers were 3 nm thin, like for the 30-layer sample shown in Figure 4b, the 90° domains formed throughout the entire structure. Obviously, the compressive epitaxial strain imposed by the cubic substrate and presumably the interfacial strains inside the ML stabilize a uniform tetragonal structure. This observation means that a strain-induced rhombohedral-to-tetragonal phase transition has occurred in the very thin PZT 60/40 layers. Interestingly, a similar observation has been made in antiferroelectric-ferroelectric SLs, as described in the following section.
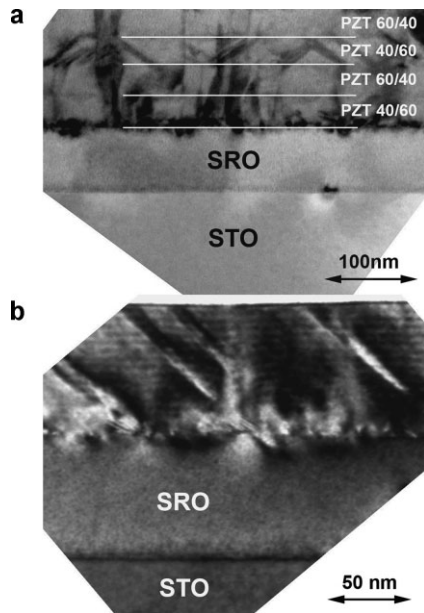
Figure 4. Cross section TEM micrographs of a) a four-layer PZT40/60/PZT60/40 heterostructure and b) a thirty-layer PZT40/60/PZT60/40 superlattice.

3.2. Antiferroelectric-Ferroelectric Multilayers and Superlattices

In view of the well-known thickness-dependent antiferromagnetic interlayer coupling effects in magnetic MLs,[33] MLs and SLs involving antiferroelectric (AFE) layers are particularly interesting with respect to the question whether thickness-dependent coupling effects can be found in these structures. The prototype antiferroelectric perovskite material is $PbZrO_3$ (PZO).[34,35] Since coupling effects in perovskite AFE/FE MLs and SLs may be expected to be largest, when coherent interfaces will be present, a ferroelectric material which is crystallographically very close to PZO was chosen to grow AFE/FE MLs and SLs, viz. ferroelectric PZT.

As a necessary prerequisite, the growth of bare PZO thin films by PLD was studied and optimized first, investigating growth-microstructure-property relations for PZO thin films of two different crystallographic orientations.[36] It was found that a characteristic P–V double hysteresis loop is recorded from the antiferroelectric PZO films due to the well-known field-induced antiferroelectric-to-ferroelectric phase transition of PZO. During this transition the crystallography of PZO changes from orthorhombic to rhombohedral.[37] In addition, at temperatures between 4 K and room temperature, in PZO films of certain crystallographic orientations a ferroelectric polarization was found in addition to the normal antiferroelectric properties.[38]

Then, a first attempt to grow epitaxial PZO/PZT multilayers, using the tetragonal PZT 20/80 composition, showed that some variation of the crystallographic orientation of PZT during growth occurred due to the rather large lattice mismatches involved at the different interfaces.[39] It was thus

decided to use the rhombohedral PZT 80/20 compositon instead of tetragonal 20/80, in order to further reduce the lattice misfit with PZO and to facilitate the formation of coherent interfaces: PZO is orthorhombic and has the lattice parameters $a = 5.88$ Å, $b = 11.787$ Å, $c = 8.231$ Å, which roughly (neglecting the atom positions) corresponds to a pseudocubic (pc) subcell with $a_{pc} = 4.137$ Å. Rhombohedral PZT has the lattice parameters $a = 4.118$ Å, $\alpha = 89.73°$, and thus is crystallographically rather close to PZO.

The following approach was taken: Three sets $[PZO_t/PZT_t]_m$ of epitaxial $PbZrO_3/Pb(Zr_{0.8}Ti_{0.2})O_3$ (PZO/PZT) MLs with a PZO/PZT-ratio of 1:1 were grown, which had an overall thickness T of 50 nm, 100 nm; and 150 nm, respectively. Here, t is the thickness (in nanometers) of the individual PZO or PZT layers, m is the number of PZO/PZT bilayers, and $T = 2 \cdot mt$. In each set of samples of a certain overall thickness T, a number of samples consisting of different number of bilayers m, corresponding to different thickness t of the individual layers, were grown. Then, microstructure – by XRD, AFM, and (HR)TEM – and properties, viz. polarization–voltage (P–V) hysteresis loops and switching current–voltage (I–V) characteristics, were studied in dependence on the thickness t of the individual layers. The MLs were prepared by layer-by-layer PLD growth on (100)-oriented vicinal $SrTiO_3$ (STO) substrates, using a KrF excimer laser at a wavelength of 248 nm. The STO substrates were chemically and thermally treated in order to achieve step-terrace structures with only one unit-cell height.[40] A conducting $SrRuO_3$ (SRO) epitaxial bottom electrode was used, and a 5 nm thick tetragonal $Pb(Zr_{0.2}Ti_{0.8})O_3$ buffer layer was deposited on top of the SRO electrode to reduce the misfit between the rhombohedral PZT and its underlayer. Pt top electrodes were deposited through a stainless steel shadow mask by rf sputtering. For more details, see Ref.[41]

Figure 5a shows a TEM cross section image of a coherently strained PZO/PZT(80/20) superlattice ($T \approx 150$ nm; $m = 8$; $t = 9$ nm) on a PZT(20/80) buffer layer and a $SrRuO_3$ electrode on a vicinal $SrTiO_3$ (100) substrate. Figure 5b is a high-resolution TEM image of part of a coherently strained superlattice with $t \approx 7$ nm, nicely showing the coherent interfaces. It turned out that in superlattices with $t > 10$ nm, the P–V
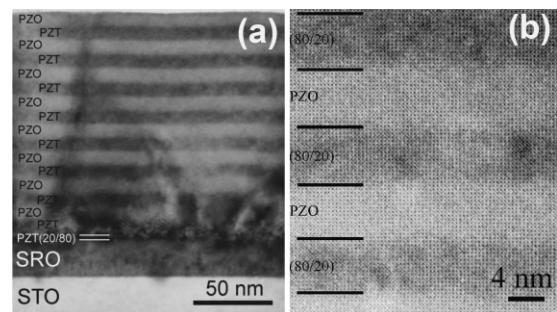

Figure 5. a) TEM cross section overview image, and b) part of a HRTEM image, of coherently strained PZO/PZT(80/20) superlattices (overall thickness 150 nm; layer thickness 9 nm and 7 nm, respectively) on a PZT(20/80) buffer layer and a $SrRuO_3$ (SRO) electrode on a vicinal $SrTiO_3$ (STO) substrate.

and *I–V* curves indicated the presence of both ferroelectricity and antiferroelectricity in the samples, which means that the PZO and PZT layers retained their AFE and FE properties, respectively. However, in superlattices with $t < 9$ nm, only ferroelectric properties were present. In other words, the very thin PZO layers underwent a field-free, most probably strain-related phase transition into a ferroelectric phase. (This is in contradiction to a previous report on PbZrO$_3$/PbTiO$_3$ epitaxial multilayers, which show only ferroelectric behavior independent of the thickness of the individual layers[42]).

XRD, in particular reciprocal space mapping, helped to understand this finding. It was shown that a sample with $t = 25$ nm shows two peaks, one for orthorhombic PZO and one for rhombohedral PZT, and another sample with $t = 6$ nm shows only one peak very close to the position of the rhombohedral peak of the first sample (Fig. 6). In a pseudocubic approximation (cf. Ref. [43]) the sample with $t = 25$ nm consists of PZO layers with $a_{pc} = 4 \times 1.0419$ Å $= 4.17$ Å and PZT layers with $a_{pc} = 4 \times 1.0331$ Å $= 4.13$ Å, so that in thick layers the PZO is under compressive, the PZT under tensile strain. After the AFE-to-FE structural phase transition of the PZO layers, both phases have $a_{pc} = 4 \cdot 1.0356$ Å $= 4.14$ Å, indicating that strain plays an important role in the thickness-related antiferroelectric-to-ferroelectric transition of the PZO layers.[41]

Discussing this transition, one should keep in mind that the component materials of the SLs have different paraelectric-to-(anti)ferroelectric transition temperatures. As a consequence, they experience successive phase transitions of this type as the stack is cooled down from the deposition temperature of 575 °C. During growth, all the layers have a cubic structure. Considering for simplicity the transition temperatures for the bulk, we expect that the para-to-ferro (cubic-to-rhombohedral) transition of the (Zr-rich) PZT layers occurs at 317 °C, and the para-to-antiferro (cubic-to-orthorhombic) transition of the PZO layers at 230 °C. A modification of the strain and electrical boundary conditions for each of the layers results at every transition temperature. In particular, in the temperature range between the transition of the (Zr-rich) PZT and that of PZO, the PZO layers are expected to be cubic and paraelectric, whereas the PZT layers are already rhombohedral and ferroelectric. The corresponding polarization charge at the interfaces may induce a non-zero electric field in the PZO layers in addition to the strain. Possibly this field helps to drive the PZO layers towards the rhombohedral ferroelectric phase. This shows that the operating mechanism may be complex and not just due to interfacial strain. However, strain should play an important role: It is well known that the FE phase in PZO thin films or single crystals can be easily induced also by stress[44,45] due to the small free energy difference between the FE and the AFE states.[46]

Apart from the described phase transition, an interesting layer thickness-dependent capacitance of these AFE/FE SLs was observed and discussed in terms of interfacial polarizations, an effect which should allow capacitance tuning in such MLs and SLs.[47]

Taken together, the two examples of ferroelectric-ferroelectric PZT 40/60/PZT 60/40 and antiferroelectric-ferroelectric PZO/PZT 80/20 SLs both demonstrate unexpected layer thickness-related property changes, which are due to thickness-dependent, most probably strain-related phase transitions. Although layer thickness-dependent dielectric and ferroelectric properties of perovskite-type MLs and SLs have been reported previously, a prominent role of strain-related phase transitions for the thickness-related property changes has most probably not been reported before.

3.3. Ferroelectric-Metal and Dielectric-Magnetostrictive Superlattices

SLs combining ferroelectric PbZr$_{0.2}$Ti$_{0.8}$O$_3$ and metallic SrRuO$_3$ (Fig. 7) were grown by PLD to be analyzed by ultrafast x-ray diffraction in pump-probe experiments, which allowed to characterize the lattice and polarization dynamics in PZT20/80 nanolayers.[48]
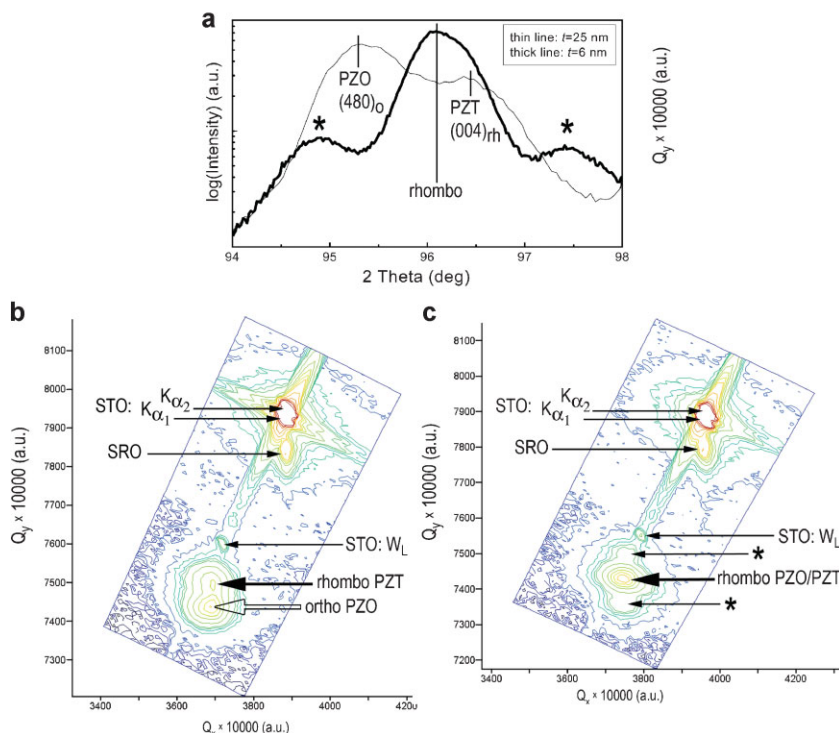

Figure 6. a) XRD θ–2θ scan ($\psi = 0°$), and b) and c) RSM plots around the (402) reflection of STO ($\psi = 26.6°$) of a sample with $t = 25$ nm (a,b) and one with $t = 6$ nm (a,c). The two peaks marked with an asterisk in (a) and (c), which are on an equal distance of $\Delta(2\theta) = 1.3°$ from the PZT(400) peak, are second-order superlattice reflections indicating a PZO/PZT layer period of 13.4 nm. Q_x and Q_y in (b) and (c) are the x and y components of the reciprocal space vector; a.u. – arbitrary units. Diffraction from the Pb(Zr$_{0.2}$Ti$_{0.8}$)O$_3$ buffer layer is not seen due to the low thickness of this layer. (Reprinted with permission from Ref. [41]. Copyright 2007, American Institute of Physics.).
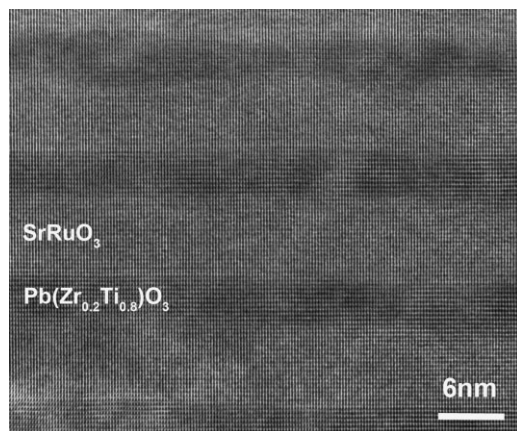
Figure 7. Cross section HRTEM of a PZT20/80/SRO superlattice with 4 nm thin PZT20/80 layers and 6 nm thin SRO layers grown on SRO/STO(100).

In particular it was shown that the spontaneous polarization within the PZT layers can be reversibly switched off by the strain induced in the $SrRuO_3$ layers, within an unexpectedly short time of 2 ps.

Similar femtosecond X-ray diffraction pump-probe experiments were performed for a different type of SL, $SrTiO_3/SrRuO_3$, having in focus the ferromagnetism exhibited by $SrRuO_3$ below 160 K and hence its magnetostrictive properties.[49] The dynamics of the observed ultrafast magnetostrictive stress generation in the $SrRuO_3$ layers have been shown to proceed on a sub-picosecond scale.

The observation of these ultrafast transition effects in the ferroelectric-metal and dielectric-magnetostrictive superlattices was certainly enabled by the coherent nature of the superlattices, which in turn was achieved by the well-controlled deposition conditions. It can be expected that further progress in studying various transition phenomena in functional perovskites on the (sub-)picosecond scale will be enabled by coherently grown superlattices with strongly controlled, suitably adapted thickness of the individual layers.

3.4. Extrinsically Multiferroic Superlattices

Another interesting class of perovskite oxides are the manganites, such as $La_xSr_{1−x}MnO_3$ (LSMO), widely investigated for the colossal magnetoresistance they exhibit close to room temperature, in the vicinity of the ferromagnetic-to-paramagnetic phase transition.[1,50–52]

In manganites intrinsic and extrinsic strain are so important that polycrystalline films, epitaxial films, powders and bulk crystals of nominally the same material may exhibit significant differences in their overall properties.[1] To contribute to a better understanding of strain-related effects in these materials, a graded heterostructure in which LSMO layers are sandwiched between layers of tetragonal PZT with increasing Zr-content were grown on STO(100) by PLD.[53] For $x \cong 0.3$, LSMO is ferromagnetic and rhombohedral below $T_C = 370$ K and its pseudo-cubic lattice parameter, $a_{pc} = 0.388$ nm, matches rather well that of $SrTiO_3$, $a = 0.3905$ nm. The LSMO layers of the same PZT/LSMO heterostructure, however, experience gradually increasing epitaxial strain due to the interfaces with PZT layers of increasing Zr-content, and thus of increasing lattice parameters. In consequence, the LSMO layers in such heterostructures undergo a gradual alteration of the coercive magnetic field. Figure 8a shows a HRTEM cross section micrograph of a heterostructure consisting of three layers of LSMO sandwiched between the STO substrate and PZT layers of various compositions. XRD, HRTEM and electron diffraction demonstrated the high structural quality of these multilayers. The magnetization hysteresis loops of a single LSMO epitaxial film grown on STO(100) and of the
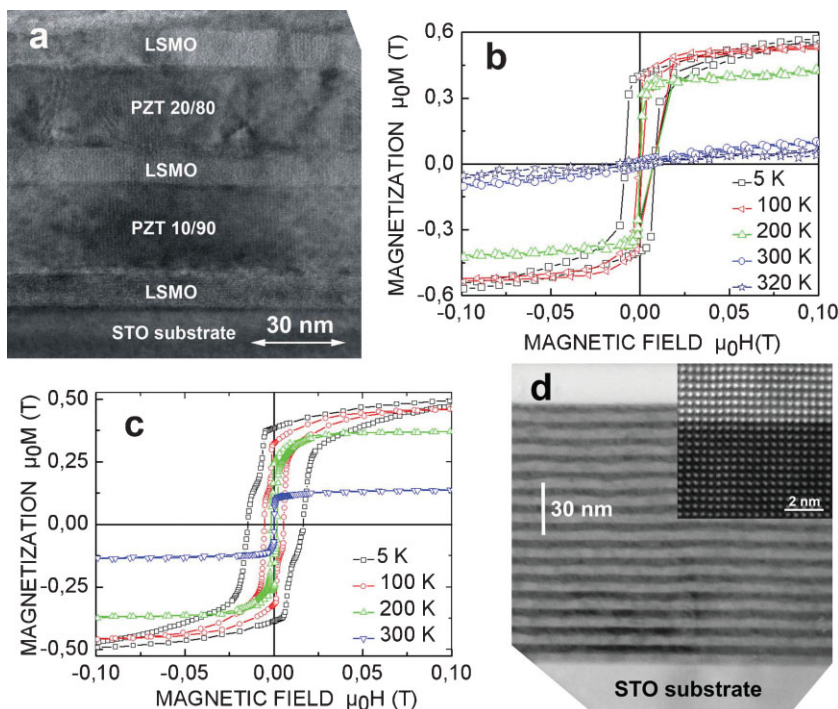
Figure 8. a) Cross section HRTEM micrograph of a six-layer PZT30/70/LSMO/PZT20/80/LSMO/PZT10/90/LSMO heterostructure grown on STO(100). In b) the magnetization hysteresis loops of a single LSMO film (5 nm thin) measured at temperatures from 5 K to 320 K are shown, and in c) magnetization hysteresis loops of the six-layer heterostructure given in (a). d) Cross section TEM micrograph of 15 PZT20/80/LSMO bilayers grown on STO(100), seen from [010] STO direction (bright layers are LSMO and dark layers are PZT20/80). The inset in (d) is a Z-contrast scanning TEM image of one of the PZT20/80/LSMO interfaces in such a multilayer. (Figs. (b),(c),(d) reprinted with permission from Ref. [53], and Fig. (a) from Ref. [97]. Copyright 2008, American Institute of Physics.).

hetrostructure shown in Figure 8a are shown in Figure 8b and c, respectively. The hysteresis loop of the 6-layer heterostructure shows several steps at different values of the magnetic field, indicating that the magnetization switches independently in each LSMO layer of the heterostructure. Presumably the LSMO layer sandwiched between the STO substrate and the PZT10/90 layer switches the magnetization first, at the lowest value of the coercive field, because this one is subjected to the lowest in-plane tensile strain (cf. Ref. [54]). Accordingly, a strain engineering of the properties of such potentially multiferroic SLs should be possible.

Heterostructures and superlattices of ferromagnetic manganites and ferroelectric perovskites, such as PZT or BaTiO$_3$, are an appealing combination, provided that the ferromagnetic and ferroelectric properties of the individual layers are retained in the SL, and, moreover, magnetoelectric coupling occurs between the layers of the SL. The very good structural match allows coherent growth with atomically flat interfaces (cf. Fig. 8d), which is a prerequisite for the study of magnetoelectric coupling and other interface-related effects. However, special attention must be paid to the growth conditions, in order to prevent interdiffusion at the interfaces, such as cation intermixing observed for a La$_{0.7}$Sr$_{0.3}$MnO$_3$/ SrTiO$_3$ multilayer, with 5 nominal unit cells for each material.[55] By electron energy-loss spectroscopy (EELS) performed in a fifth-order aberration-corrected scanning transmission electron microscope, Ti was found to diffuse into the LSMO layers and Mn into the STO layers, and also a low concentration of La was detected inside the SrTiO$_3$ layers. The changes measured for the titanium bonding as the local environment changed allowed Muller et al.[55] to discriminate between chemical interdiffusion and possible imaging artifacts. The cation intermixing may play an important role in intriguing phenomena reported for such multilayers. Dörr et al.[56] observed that for coherently grown La$_{0.7}$Sr$_{0.3}$MnO$_3$/SrTiO$_3$ multilayers with LSMO layers thinner than ca. 8 unit cells a pronounced drop in the ferromagnetic Curie temperature occurred, accompanied by a strong increase of the coercive field, and the in-plane electrical transport changed from metallic to insulating, for multilayers with LSMO layers thinner than 2.3 nm.[56,57] Again these observations demonstrate the wealth of physical effects which can be expected from the reduction of the individual layer thickness in functional perovskite multilayers and superlattices.

4. Intrinsically Multiferroic Epitaxial Films

Bismuth ferrite, BiFeO$_3$ (BFO), is a perovskite that acutely revived the interest in intrinsic multiferroic materials, i.e., materials that exhibit coexistence of at least two ferroic orders (ferroelectric, ferroelastic, and ferromagnetic).[2,58–60] As an exciting advantage over some manganites that show multiferroicity at low temperatures,[61] BFO is a room temperature (RT) multiferroic with the ferroelectric Curie temperature ($T_C = 820\,°C$) and the antiferromagnetic Néel temperature ($T_N = 370\,°C$) both far above RT. The interest in BFO was further enhanced by the achievement of single-phase BiFeO$_3$ epitaxial films exhibiting large ferroelectric polarization at RT by the group of Ramesh in Berkley.[59] The growth of single-phase BiFeO$_3$ films is by no means easy. Bismuth ferrite films have often been reported to contain impurity phases, such as bismuth oxide (Bi$_2$O$_3$), iron oxide (α-, γ-Fe$_2$O$_3$),[62,63] or non-stoichiometric phases, such as Bi$_{25}$FeO$_{39}$,[64] strongly dependent on the synthesis conditions and dramatically affecting the measured ferroelectric and ferromagnetic properties. Ramesh's Berkley group grew BFO films either on single crystal substrates such as SrTiO$_3$ and DyScO$_3$, or on SrTiO$_3$-buffered Si wafers, and also varied the substrate orientation in order to obtain BFO(100)-, (110)-, or (111)-oriented films. The RT spontaneous polarization of epitaxial BFO(111) films was up to 90–95 μC cm^{-2}, consistent with first-principle predictions.[65] Thus the polarization in the lead-free BFO competes with the highest values measured in epitaxial tetragonal PZT films.[15,17–20,66]

Figure 9 shows the atomic force microscopy (AFM) image of the surface and TEM cross section micrograph of an epitaxial BFO film (ca. 170 nm thick) grown on SrRuO$_3$-coated DyScO$_3$(110) by PLD at MPI Halle.[67] Saturated ferroelectric hysteresis loops could be measured at room temperature employing Pt/SRO top electrodes (60-μm-size squares) and the remnant polarization was ca. 55 μC cm^{-2} at 2 kHz.

BFO has been readily envisaged as a candidate for devices based on magnetoelectric coupling at RT, by combining multiferroic BFO with ferromagnetic layers such as (La,Sr)MnO$_3$[68] and NiFe.[69] An approach for the electrical
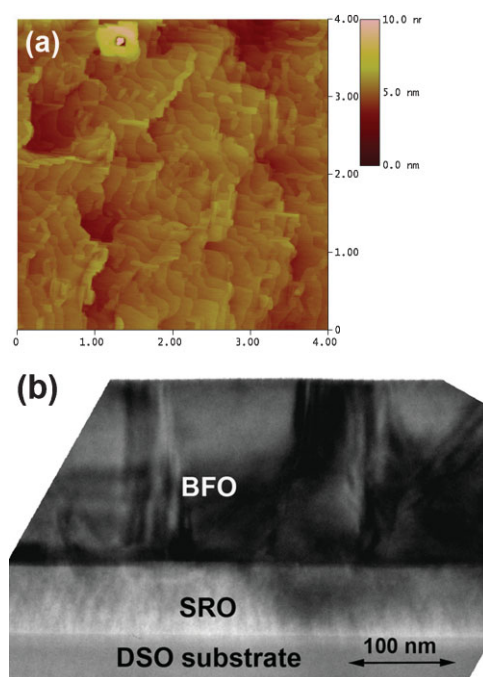

Figure 9. AFM topography image of a 175 nm BiFeO$_3$ film (4 x 4 μm^2) and cross section TEM of this film grown on a SrRuO$_3$-coated DyScO$_3$ (110) substrate (Ref. [67]).

control of ferromagnetism was proposed in BFO/ferromagnetic bilayers, exploiting the simultaneous intrinsic multiferroic coupling between the ferroelectricity and antiferromagnetism in the BFO layer and the extrinsic exchange coupling between the ferromagnetic layer and the antiferromagnetic BFO.[2,59]

5. Nanoscale Ferroelectrics

In the last decade a large effort has been made to investigate size effects in nanoscale ferroelectrics. For the two-dimensional systems, viz. ultrathin films, the limit at which ferroelectricity would disappear has been established theoretically and experimentally to be only a few unit cells.[70,71] The experimental investigations of only a few unit cells thick complex oxide films became possible due to advanced techniques of film deposition, which nowadays yield high-quality well controlled single crystal films. Nonetheless, in real life usually laterally structured films, respectively patterned structures, are used to define devices in which the ferroelectric films might be only one (active) part. This additional patterning process has two major implications on ferroelectric properties. Firstly, patterning a complex material down to the nanoscale range is technically not a trivial task. Secondly and more important, from the basic physics the volume of the patterned structure is now limited in all three dimensions and eventual size effects are expectedly more severe than in the laterally extended film case.

The following section will address patterning of nanoscale ferroelectric structures, respectively structures with all dimensions in the sub-100-nm range, as well as significant effects that are size-related and which might affect ferroelectricity at the nanoscale.

5.1. Self-Assembled Nanoscale Structures

A classical top-down patterning processing starts with a thin film, and structures of desired geometry are carved in it using photolithography and etching. There are obvious advantages of this process, one being the starting "material" itself, which can be a high-quality, well controlled and characterized thin film, along with the possibility of large area processing and controlled size and positioning. Nevertheless, etching a complex material such as PZT or other ternary/quaternary perovskite oxides has been proven to be a complex task. The etching process usually renders a damaged region at the rim of the patterned structure which, depending on the particular process, can be as large as the final structures.[72,73]

The only way to avoid the expensive top-down processes is to develop self-assembly processes which would allow to pattern large area arrays of high-quality, possibly epitaxial, nanostructures with lateral dimensions at the nanoscale, respectively in the sub-100 nm range. Epitaxial structures are particularly useful to establish those factors that might influence the ferroelectric behavior at the nanoscale. The epitaxial character of the patterned nanostructures would

result in a single orientation of all structures, which consequently will give the possibility of in-depth structural analysis using standard macroscopic methods such as X-ray diffraction, and will enable to understand the role of structural defects for the electrical and optical properties.

One of the possibilities is based on the analysis of ultrathin film growth by chemical solution deposition (CSD).[74] It was noticed that it is rather difficult to grow perovskite ultrathin films starting with amorphous precursor films due to local instabilities that occur at the crystallization stage. As the precursor film thickness decreases and the crystallization temperature increases, the crystallized film splits and eventually breaks into small crystallites. The effect is caused by the total surface and interface energy, which is minimized by introducing surfaces of lower energy into the substrate-film system. For instance, in the $PbTiO_3$–$SrTiO_3$ (001) system, additional crystallographic planes, respectively (110) and (111), with lower energy than the interface and surface epitaxial (001) plane are being introduced.

We have used this method to fabricate large-area arrays of epitaxial ferroelectric nanosize structures. Briefly, an ultrathin amorphous film is deposited on a single-crystal substrate by spin-coating an appropriate precursor solution, followed by a simple pyrolyse process at temperatures of about 300 °C. The nanosize structures are formed by a high temperature annealing, e.g., at 900 °C for one hour. During the final annealing the amorphous film breaks up and due to enhanced surface mobility forms islands that eventually crystallize. The final dimension of the structures is related to the initial thickness of the amorphous layer, the final annealing temperature, and the annealing time. The method is flexible and can be used virtually on any substrate. The main driving force for island formation, viz. the minimization of the total interface and surface energy, acts irrespective of the nature of the substrate underneath. If the substrate is polycrystalline, the orientation of the structures is random and this might influence the analysis of the data subsequently acquired.[75,76]

We used the above method to fabricate epitaxial PZT structures with different shapes and sizes. We noticed that the misfit between the substrate and the grown structures influences the final shape. A large misfit usually results in small structures, whereas a small misfit generates irregular shapes and a larger size distribution. TEM and HRTEM analysis of the obtained structures showed a high crystal quality, a good thickness uniformity over a large area, and a narrow size distribution of the nanostructures. All structures have a truncated pyramid shape with atomically flat surfaces and are free from extended defects, except for interfacial misfit dislocations, which relax the strain caused by the misfit between the substrate and the epitaxial structure (Fig. 10). In the case of PZT52/48 islands on STO the distance between the dislocations is from 9 nm to 13 nm, in agreement with the calculated spacing, which is about 12 nm. Actually, a network of misfit dislocations having an average mutual distance of about 12 nm developed at the interface as shown by the plan-view TEM image in Figure 10b.
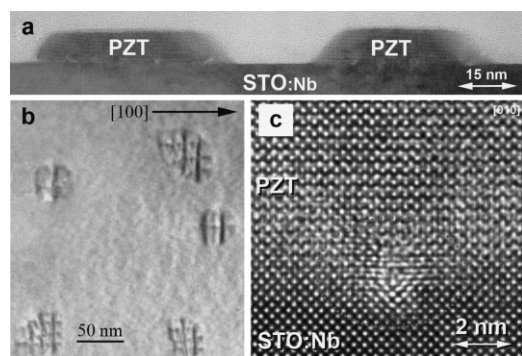
Figure 10. a) TEM cross section image of two PZT52/48 nanoscale structures grown on STO:Nb substrate; b) plan-view image of similar structures as in (a), showing the misfit dislocation network in the self-assembled islands; c) Cross sectional HRTEM image revealing contrast due to a misfit dislocation of in-plane Burgers vector $\mathbf{b} = a\langle 100 \rangle$. For details, see Ref. [10].

Figure 11. a) Topography (wire frame) and frozen-active layer interface (solid surface). The frozen layer thickness varies from 0 to 20% of the dot thickness. b) Map of the corresponding imprint bias for the switchable part of the nanoisland. (After Ref. [77]).

This network of dislocations was proven to be detrimental for the ferroelectric properties as mentioned shortly in Section 2.1. A region of high strain is present around the dislocation core, which extends into the volume of the ferroelectric nanostructure. The analysis of HRTEM images revealed a strain of about 3.5%, which is almost the same value as the tetragonality of the PZT unit cell and which extends only into the PZT layer.[10] Consequently the ferroelectricity in the highly strained volume around the dislocation core is negatively affected. If this disturbed volume is sufficiently large compared to the entire volume of the nanostructure, e.g., more than about 60%, the ferroelectric properties are severely affected even leading to the disappearance of ferroelectric properties. Avoiding the formation of misfit dislocations either by substrate engineering or by choosing an appropriate composition of PZT mitigates this effect and in certain cases will lead to the reappearance of ferroelectricity. This extrinsic size effect based on extended lattice defects is not particular to nanostructures. It is valid also for thin and ultrathin films where the thickness is just above the critical value and misfit dislocations and threading dislocations occur.

The above self-patterned nanoscale structures have been a good platform for in-depth investigations of the effects induced by defects, making use of the newly developed scanning spectroscopy piezoresponse force microscopy (SS-PFM). Rodriguez et al. showed a notable spatial distribution of the switching behavior within a single ferroelectric epitaxial nanostructure.[77] 2D maps of switching properties (Fig. 11) revealed an inactive layer within the nanostructure that causes a variation of the switching activity, including coercive bias, imprint, remanent electromechanical responses, and work of switching. SS-PFM enabled quantifying and mapping, with nanoscale resolution, the influence of misfit dislocations on switching properties.

The self-assembled epitaxial nanoscale structures enabled us to correlate the size effects to the structural quality. It has been shown that interface and surface related defects, as well as extended defects, might play a more detrimental role than had
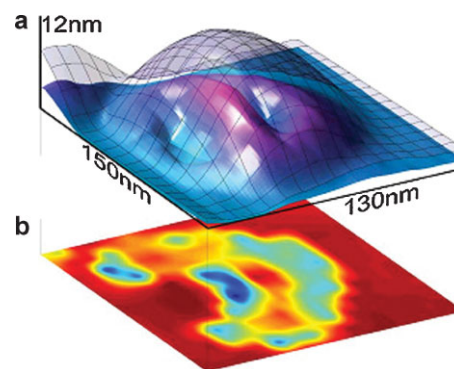
been recognized before. Additionally, it was shown that analyses of the size effects without a complex structural, electrical and optical analysis might be erroneous. However, considering practical purposes, two features were not yet achieved: i) geometrical order of the array, and ii) patterning of metal-ferroelectric-metal (MFM) capacitors.

5.2. Geometrically Ordered Arrays

To achieve well-ordered arrays of nanoscale ferroelectric structures without using the classic top-down process is technically very demanding. On a more mesoscopic scale, arrays of ferroelectric structures have been prepared by electron-beam direct writing.[78] and imprint lithography.[79] Both methods are, however, limited in size. On a truly nanoscopic scale, one idea to prepare arrays was based on the substrate-strain mediated spontaneous ordering of nanostructures.[80,81] The hope was that periodic pits imprinted into the surface of the substrate would help in achieving a well-ordered arrangement of the nanoscale structures. Using a mask comprising a regular array of silicon nitride pyramids with a sub-micrometer periodicity, the as-deposited amorphous precursor layer was imprinted. Unfortunately this did not result in the desired order, but rather in an increase of both the distance between the structures and the average dimension. This is due most probably to the large mismatch between the pitch of the imprint mask and the average distance between the self-assembled nanostructures.[82]

An alternative method is to use a stencil mask and to deposit the ferroelectric material onto the substrate of choice through this mask. The stencil mask may in turn be fabricated using self-assembly methods. Ma and Hesse used monolayers of latex spheres as stencil mask to deposit (by PLD) amorphous $BaTiO_3$ and $SrBi_2Ta_2O_9$ islands through the free spaces.[83–85] After lift-off and crystallization annealing, regular hexagonally arranged structures were obtained (Fig. 12), which in case of $BaTiO_3$ were epitaxial.[83] Size and pitch of the structures were determined chiefly by the diameter of the latex spheres. For a
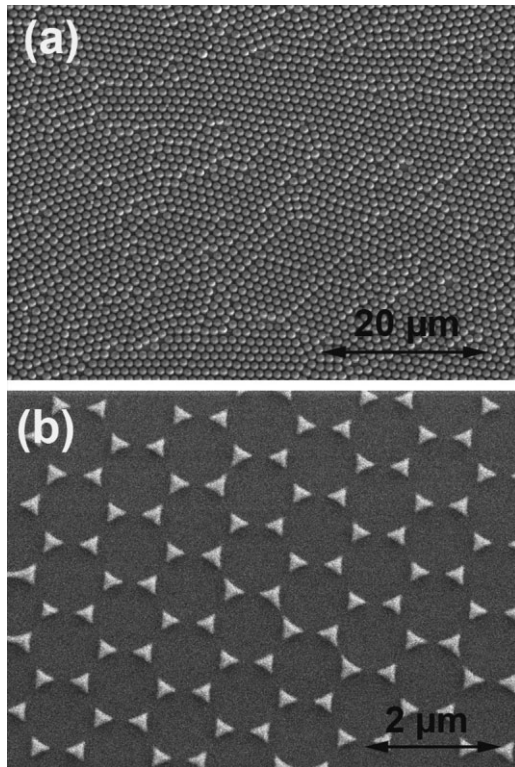
Figure 12. a) Latex–sphere based stencil mask, b) Ferroelectric SrBi$_2$Ta$_2$O$_9$ nanostructures obtained after PLD deposition and lift-off. (After Refs. [83, 85]).

Figure 13. a) Gold membrane used as stencil mask for PZT deposition. The inset shows a close-up SEM image of the membrane rim, with a detail of single Au nanotubes; b) Perfectly ordered PZT epitaxial nanostructure array obtained after deposition, mechanically lifting off the Au membrane, and high-temperature annealing. The inset shows a typical PFM hysteresis loop acquired on a single nanostructure. (After Ref. [86]).

diameter of the latex spheres of one micrometer, the pitch and lateral size were 500 nm and 300 nm, respectively (see Fig. 12b). Again, the substrate played an important role in establishing the final crystal quality of the patterned structures. SRO-buffered STO substrates yielded high-quality epitaxial structures with good ferroelectric properties.

Although the method is quite easy and elegant, it suffers from a few disadvantages; among the most important are the lack of long range order, and the final size of the individual nanostructures. Latex spheres are self-organizing in hexagonal symmetry but in rather small domains, as shown in Figure 12a. Nevertheless, the work has opened the possibility to use PLD-based deposition methods in combination with lift-off masks to fabricate epitaxial nanostructures.

The next steps we undertook were aiming towards improving the long-range order and decreasing the lateral size of the structures. Lee et al.[86] have developed an alternative mask, based on a self-assembly process. They used porous anodic alumina (AAO) as template and electrodeposition to fabricate gold nanotube membranes (Fig. 13) which later on have been used as stencil mask for the deposition of ferroelectric nanostructures.[86]

Perfectly ordered lanthanum-doped bismuth titanate (BLT), strontium bismuth tanatalate (SBT), and PZT nanostructures were fabricated on large area substrates
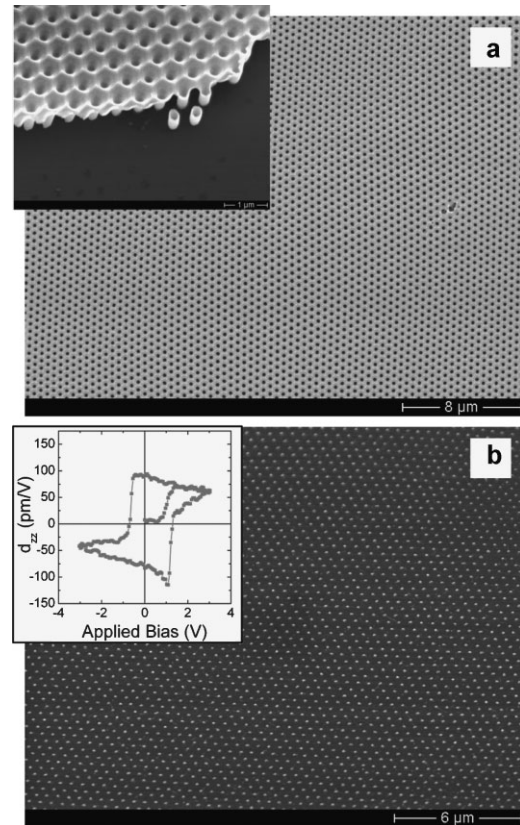
(typically 1 cm^2) by deposition of ferroelectric material through the Au nanotube membrane.[87] PLD deposition was performed again at room temperature, to avoid damage of the gold mask. The periodic arrangement, on large area, of the Au nanotube membranes is determined by the AAO template. Perfectly ordered, large-area AAO templates having either hexagonal, quadratic, or complex Moire-type symmetry were achieved by controlling the anodization process of aluminium using imprint methods.[88] After mechanical lift-off of the membrane and high temperature crystallization, epitaxial BLT nanostructures with a height of about 100 nm and a lateral size of about 150 nm were obtained. Using substrates with different crystallographic orientation, epitaxial BLT nanostructures with different orientations could be achieved.[89] Besides local investigations of the switching properties, the large area and periodic arrangement of the nanostructures enabled detailed macroscopic structural investigations based on usual laboratory-based x-ray diffraction analysis, showing that the large area is important to determine structural properties using macroscopic-size samples consisting of many mostly identical nanostructures.[89]

5.3. Metal-Ferroelectric-Metal Nanocapacitor Arrays

Although the patterning method based on Au nanotube membranes is a versatile method providing large-area arrays with perfectly periodic arrangement of the nanostructures and a wide range of structure dimensions and pitches, there are two main disadvantages: i) the impossibility to grow the structures directly in epitaxial form, and consequently, ii) the impossibility to deposit dissimilar crystalline materials in the same run, i.e., using the same mask. As a result, nanoscale ferroelectric capacitors, or any other complex multilayered structures, can not be achieved due to the high temperature anneal needed to crystallize the ferroelectric. In order to overcome this deficiency, Lee et al. have developed a fabrication method based on ultrathin AAO membranes.[90] Instead of using gold nanotube membranes as lift-off masks, ultrathin AAO membranes are used. Due to the high temperature stability of the Al_2O_3 mask, PLD deposition can be performed at relatively high temperatures. Thus epitaxial ferroelectric nanostructures can be directly obtained. Moreover, since the crystallization annealing is not anymore necessary, multiple subsequent depositions of dissimilar materials can be easily performed. This has been recently demonstrated, obtaining well-ordered nanoscale Pt–PZT–Pt capacitor arrays with a density approaching terabit/inch^2. The epitaxially grown capacitors are randomly addressable and possess good switching properties, as shown by piezoresponse-AFM.[90]

Figure 14 shows part of such a well-ordered array of Pt–PZT–Pt nanocapacitors with almost terabit inch^{-2} density, grown by PLD at respective high deposition temperatures
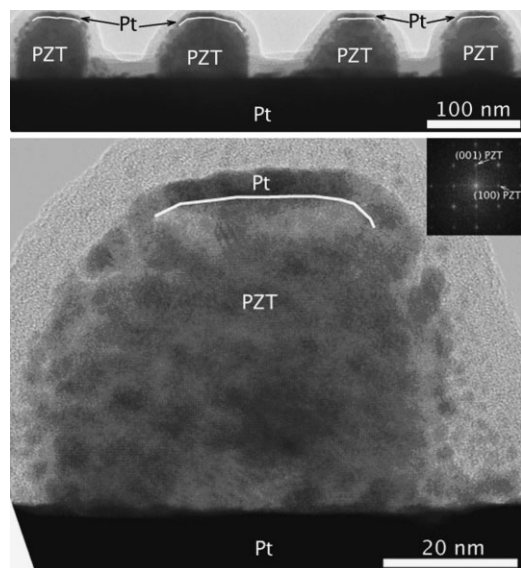

Figure 14. TEM cross section images of (top) part of a well-ordered array of Pt/PZT/Pt nanocapacitors with almost terabit/inch^2 density, and (bottom) a single capacitor. The inset in the bottom picture shows a Fourier transform of the PZT island, demonstrating the PZT epitaxy. The dotted contrast of PZT and Pt is most probably due to the focussed ion-beam thinning process. (After Ref. [90]).

using an AAO mask of high temperature stability, as well as one of the capacitors at higher magnification.

6. Extrinsically Multiferroic Composite Nanostructures

Extrinsically multiferroic, epitaxial columnar nanostructures of ferrimagnetic spinel phases (e.g., $CoFe_2O_4$, $NiFe_2O_4$) and ferroelectric perovskite phases (e.g., $BaTiO_3$, $BiFeO_3$, $PbTiO_3$) were fabricated by PLD from mixed spinel-perovskite targets, making use of the self-assembly and spontaneous phase-separation processes undergone by the two phases during the subsequent film growth.[91–93] In the case of $CoFe_2O_4$-$BiFeO_3$ nanocomposite epitaxial films, by selecting single-crystal substrates with different orientation (e.g., $SrTiO_3$(100) or (111)), the shape and the phase that forms nanopillars embedded in the matrix of the other phase can be controlled.[94] Electric field induced magnetization switching was reported for such $(CoFe_2O_4)_{0.35}$–$(BiFeO_3)_{0.65}$ multiferroic structures and thus the possibility for electrically assisted magnetic recording was envisaged in multiferroic systems with such high perpendicular magnetic anisotropy.[95,96] The magnetization reversal process in $CoFe_2O_4$ was described as a result of the polarization switching in the $BiFeO_3$ matrix subsequent to the application of an electric field. The ferroelectromagnetic coupling in these heterostructures is a result of strain interaction due to the piezoelectric and magnetistrictive properties of the two phases, respectively. However, to reach the stage of the feasibility of the proposed electrically assisted magnetic recording scheme, the $CoFe_2O_4$ pillars that define the individual bits should have dimensions well below 100 nm, and well-ordered arrays must be achieved. The methods described in Section 5.2 to prepare well-ordered arrays of nanostructures should also be suitable for the preparation of well-ordered arrays of nanoscopic multiferroic heterostructures.

7. Conclusion

Functional perovskite oxides represent a particular class of functional materials with a tremendous variety of interesting and useful properties. Among them are, e.g., (anti)ferroelectric, (anti)ferromagnetic, piezoelectric, magnetostrictive, and conducting perovskites. In recent years, the growth of epitaxial films, multilayers, superlattices, laterally nanostructured films and arrays of well-ordered nanostructures from functional perovskites has considerably developed, to such an extent that in many cases rather perfect structures have been grown. On one hand, this allowed to study growth-microstructure-property relations for many perovskites in previously not known detail. On the other hand this enabled, and will further enable, the growth of one-, two-, and three-dimensional heterostructures on the nanoscale, combining different

perovskites with various properties, thus achieving novel structures with new or unconventional properties. No doubt, this process will further develop, and we are looking forward to learn about new achievements in the near future.

[1] C. Israel, M. J. Calderón, N. D. Mathur, *Mater. Today* **2007**, *10*, 24.

[2] R. Ramesh, N. A. Spaldin, *Nat. Mater.* **2007**, *6*, 21.

[3] H. U. Habermeier, *Mater. Today* **2007**, *10*, 34.

[4] H. Ohta, *Mater. Today* **2007**, *10*, 44.

[5] C. B. Eom, A. F. Marshall, S. S. Laderman, R. D. Jacowitz, T. H. Geballe, *Science* **1990**, *249*, 1549.

[6] H. N. Lee, D. Hesse, N. Zakharov, U. Gösele, *Science* **2002**, *296*, 2006.

[7] S. P. Alpay, I. B. Misirlioglu, V. Nagarajan, R. Ramesh, *Appl. Phys. Lett.* **2004**, *85*, 2044.

[8] V. Nagarajan, C. L. Jia, H. Kohlstedt, R. Waser, I. B. Misirlioglu, S. P. Alpay, R. Ramesh, *Appl. Phys. Lett.* **2005**, *86*, 192910.

[9] I. B. Misirlioglu, S. P. Alpay, M. Aindow, V. Nagarajan, *Appl. Phys. Lett.* **2006**, *88*, 102906.

[10] M. W. Chu, I. Szafraniak, C. Harnagea, R. Scholz, D. Hesse, M. Alexe, U. Gösele, *Nat. Mater.* **2004**, *3*, 87.

[11] C. L. Canedy, H. Li, S. P. Alpay, L. Salamanca-Riba, A. L. Roytburd, R. Ramesh, *Appl. Phys. Lett.* **2000**, *77*, 1695.

[12] D. Balzar, P. A. Ramakhrishnan, P. Spagnol, S. Mani, A. M. Hermann, A. M. Matin, *Jpn. J. Appl. Phys. Part 1* **2002**, *41*, 6628.

[13] L. Ryen, X. Wang, P. Petrov, E. Carlsson, U. Helmerrson, E. Olsson, *J. Appl. Phys.* **1999**, *85*, 3976.

[14] I. Vrejoiu, G. Le Rhun, N. D. Zakharov, D. Hesse, L. Pintilie, M. Alexe, *Philos. Mag.* **2006**, *86*, 4477.

[15] I. Vrejoiu, G. Le Rhun, L. Pintilie, D. Hesse, M. Alexe, U. Gösele, *Adv. Mater.* **2006**, *18*, 1657.

[16] W. Hong, H. N. Lee, M. Yoon, H. M. Christen, D. H. Lowndes, Z. Suo, Z. Zhang, *Phys. Rev. Lett.* **2005**, *95*, 095501.

[17] L. Pintilie, I. Vrejoiu, D. Hesse, G. LeRhun, M. Alexe, *Phys. Rev. B* **2007**, *75*, 224113.

[18] L. Pintilie, I. Vrejoiu, D. Hesse, G. LeRhun, M. Alexe, *Phys. Rev. B* **2007**, *75*, 104103.

[19] V. Nagarajan, J. Junquera, J. Q. He, C. L. Jia, R. Waser, *J. Appl. Phys.* **2007**, *100*, 051609.

[20] H. N. Lee, S. M. Nakhmanson, M. F. Chisholm, H. M. Christen, K. M. Rabe, D. Vanderbilt, *Phys. Rev. Lett.* **2007**, *98*, 217602.

[21] K. J. Choi, M. Biegalski, Y. L. Li, A. Sharan, J. Schubert, R. Uecker, P. Reiche, Y. B. Chen, X. Q. Pan, V. Gopalan, L.-Q. Chen, D. G. Schlom, C. B. Eom, *Science* **2004**, *306*, 1005.

[22] J. F. Scott, C. A. P. de Araujo, *Science* **1989**, *246*, 1400.

[23] W. Pompe, X. Gong, Z. Suo, J. S. Speck, *J. Appl. Phys.* **1993**, *74*, 6012.

[24] G. Le Rhun, I. Vrejoiu, L. Pintilie, D. Hesse, M. Alexe, U. Gösele, *Nanotechnology* **2006**, *17*, 3154.

[25] G. Le Rhun, I. Vrejoiu, M. Alexe, *Appl. Phys. Lett.* **2007**, *90*, 012908.

[26] V. Nagarajan, A. Roytburd, A. Stanishevsky, S. Prasertchoung, T. Zhao, L. Chen, J. Melngailis, O. Auciello, R. Ramesh, *Nat. Mater.* **2003**, *2*, 43.

[27] S. Jesse, B. J. Rodriguez, S. Choudhury, A. P. Baddorf, I. Vrejoiu, D. Hesse, M. Alexe, E. A. Eliseev, A. N. Morozovska, J. Zhang, L. Q. Chen, S. V. Kalinin, *Nat. Mater.* **2008**, *7*, 209.

[28] C.-L. Jia, S. B. Mi, K. Urban, I. Vrejoiu, M. Alexe, D. Hesse, *Nat. Mater.* **2008**, *7*, 57.

[29] H. N. Lee, H. M. Christen, M. F. Chisholm, C. M. Rouleau, D. H. Lowndes, *Nature* **2004**, *433*, 395.

[30] M. Dawber, N. Stuki, C. Lichtensteiger, S. Gariglio, P. Ghosez, J.-M. Triscone, *Adv. Mater.* **2007**, *19*, 4153.

[31] Y. L. Li, S. Y. Hu, D. Tenne, *Appl. Phys. Lett.* **2007**, *91*, 252904.

[32] I. Vrejoiu, Y. L. Zhu, G. Le Rhun, M. A. Schubert, M. Alexe, D. Hesse, *Appl. Phys. Lett.* **2007**, *90*, 072909.

[33] D. H. Mosca, F. Petroff, A. Fert, P. A. Schroeder, W. P. Pratt, Jr, R. Laloee, *J. Magn. Magn. Mater.* **1991**, *94*, L1.

[34] E. Sawaguchi, G. Shirane, Y. Takagi, *J. Phys. Soc. Jpn.* **1951**, *6*, 333.

[35] G. Shirane, E. Sawaguchi, Y. Takagi, *Phys. Rev.* **1951**, *84*, 476.

[36] K. Boldyreva, D. H. Bao, G. Le Rhun, L. Pintilie, M. Alexe, D. Hesse, *J. Appl. Phys.* **2007**, *102*, 044111.

[37] O. E. Fesenko, R. V. Kolesova, Y. G. Sindeyev, *Ferroelectrics* **1978**, *20*, 177.

[38] L. Pintilie, K. Boldyreva, M. Alexe, D. Hesse, *J. Appl. Phys.* **2008**, *103*, 024101.

[39] D. H. Bao, R. Scholz, M. Alexe, D. Hesse, *J. Appl. Phys.* **2007**, *101*, 054118.

[40] G. Koster, B. L. Kropman, G. J. H. M. Rijnders, D. H. A. Blank, H. Rogalla, *Appl. Phys. Lett.* **1998**, *73*, 2920.

[41] K. Boldyreva, L. Pintilie, A. Lotnyk, I. B. Misirlioglu, M. Alexe, D. Hesse, *Appl. Phys. Lett.* **2007**, *91*, 122915.

[42] I. Kanno, S. Hayashi, R. Takama, T. Hirao, *Appl. Phys. Lett.* **1996**, *68*, 328.

[43] F. Jona, G. Shirane, F. Mazzi, R. Pepinsky, *Phys. Rev.* **1957**, *105*, 849.

[44] M. P. Moret, J. J. Schremer, F. D. Tichelaar, E. Aret, P. R. Hageman, *J. Appl. Phys.* **2001**, *92*, 3947.

[45] V. Yu. Topolov, A. V. Turik, O. E. Fesenko, V. V. Eremkin, *Ferroelectrics Lett. Sect.* **1995**, *20*, 19.

[46] E. Sawaguchi, *J. Phys. Soc. Jpn.* **1953**, *81*, 615.

[47] L. Pintilie, K. Boldyreva, M. Alexe, D. Hesse, *New J. Phys.* **2008**, *10*, 013003.

[48] C. von Korff Schmising, M. Bargheer, M. Kiel, N. Zhavoronkov, M. Woerner, T. Elsaesser, I. Vrejoiu, M. Alexe, D. Hesse, *Phys. Rev. Lett.* **2007**, *98*, 257601.

[49] C. von Korff Schmising, A. Harpoeth, N. Zhavoronkov, Z. Ansari, M. Woerner, T. Elsaesser, M. Bargheer, M. Schmidtbauer, I. Vrejoiu, M. Alexe, D. Hesse, *Phys. Rev. B* **2008**, *78*, 060404(R).

[50] R. von Helmolt, J. Wecker, B. Holzapfel, L. Schultz, K. Samwer, *Phys. Rev. Lett.* **1993**, *71*, 2331.

[51] A. Urushibara, Y. Moritomo, T. Arima, A. Asamitsu, G. Kido, Y. Tokura, *Phys. Rev. B* **1995**, *51*, 14103.

[52] J. Fontcuberta, B. Martinez, A. Seffar, S. Pinol, J. L. Garcia Munoz, *Phys. Rev. Lett.* **1996**, *76*, 1122.

[53] I. Vrejoiu, M. Ziese, A. Setzer, B. I. Birajdar, A. Lotnyk, M. Alexe, D. Hesse, *Appl. Phys. Lett.* **2008**, *92*, 152506.

[54] M. Przybylski, J. Grabowski, F. Zavaliche, W. Wulfhekel, R. Scholz, J. Kirschner, *J. Phys. D* **2002**, *35*, 1821.

[55] D. A. Muller, L. Fitting Kourkoutis, M. Murfit, J. H. Song, H. Y. Hwang, J. Silcox, N. Dellby, O. L. Krivanek, *Science* **2008**, *319*, 1073.

[56] K. Dörr, T. Walter, M. Sahana, K.-H. Müller, K. Nenkov, K. Brand, L. Schultz, *J. Appl. Phys.* **2001**, *89*, 6973.

[57] M. Izumi, Y. Ogimoto, Y. Okimoto, T. Manako, P. Ahmet, K. Nakajima, T. Chikyow, M. Kawasaki, Y. Tokura, *Phys. Rev. B* **2001**, *64*, 064429.

[58] W. Eerenstein, N. D. Mathur, J. F. Scott, *Nature* **2006**, *442*, 759.

[59] Y.-H. Chu, L. W. Martin, M. B. Holcomb, R. Ramesh, *Mater. Today* **2007**, *10*, 16.

[60] C. W. Nan, M. I. Bichurin, S. Dong, D. Viehland, G. Srinivasan, *J. Appl. Phys.* **2008**, *103*, 031101.

[61] M. Fiebig, T. Lottermoser, D. Fröhlich, A. V. Goltsev, R. V. Pisarev, *Nature* **2002**, *419*, 818.

[62] H. Bea, M. Bibes, A. Barthélémy, K. Bouzehouane, E. Jacquet, A. Khodan, J.-P. Contour, *Appl. Phys. Lett.* **2005**, *87*, 072508.

[63] S. H. Lim, M. Murakami, W. L. Sarney, S. Q. Ren, A. Varatharajan, V. Nagarajan, S. Fujino, M. Wuttig, I. Takeuchi, L. G. Salamanca-Riba, *Adv. Funct. Mater.* **2007**, *17*, 2594.

[64] R. Palai, R. S. Katiyar, H. Schmid, P. Tissot, S. J. Clark, J. Robertson, S. A. T. Redfern, G. Catalan, J. F. Scott, *Phys. Rev. B* **2008**, *77*, 014110.

[65] J. B. Neaton, C. Ederer, U. V. Waghmare, N. A. Spaldin, K. M. Rabe, *Phys. Rev. B* **2005**, *71*, 014113.

[66] H. S. Morioka, S. Yokoyama, T. Oikawa, H. Funakubo, K. Saito, *Appl. Phys. Lett.* **2004**, *85*, 3516.

[67] I. Vrejoiu, B. I. Birajdar, B. J. Rodriguez, D. Hesse, M. Alexe, unpublished.

[68] H. Bea, M. Bibes, M. Sirena, G. Herranz, K. Bouzehouane, E. Jacquet, S. Fusil, P. Paruch, M. Dawber, J.-P. Contour, A. Barthélémy, *Appl. Phys. Lett.* **2006**, *88*, 062502.

[69] J. H. Dho, X. Qi, H. Kim, J. L. MacManus-Driscoll, M. G. Blamire, *Adv. Mater.* **2006**, *18*, 1445.

[70] D. D. Fong, G. B. Stephenson, S. K. Streiffer, J. A. Eastman, O. Auciello, P. H. Fuoss, C. Thompson, *Science* **2004**, *304*, 1650.

[71] J. Junquera, P. Ghosez, *Nature* **2003**, *422*, 506.

[72] A. Stanishevsky, B. Nagaraj, J. Melngailis, R. Ramesh, L. Khriachtchev, E. McDaniel, *J. Appl. Phys.* **2002**, *92*, 3275.

[73] A. Stanishevky, S. Aggarwal, A. S. Prakash, J. Melngailis, R. Ramesh, *J. Vac. Sci. Technol. B* **1998**, *16*, 3899.

[74] A. Seifert, A. Vojta, J. S. Speck, F. F. Lange, *J. Mater. Res.* **1996**, *11*, 1470.

[75] R. Waser, T. Schneller, S. Hoffmann-Eifert, P. Ehrhart, *Integr. Ferroelectr.* **2001**, *36*, 3.

[76] A. Roelofs, T. Schneller, K. Szot, R. Waser, *Appl. Phys. Lett.* **2002**, *81*, 5231.

[77] B. J. Rodriguez, S. Jesse, M. Alexe, S. V. Kalinin, *Adv. Mater.* **2008**, *20*, 109.

[78] M. Alexe, C. Harnagea, D. Hesse, U. Gösele, *Appl. Phys. Lett.* **1999**, *75*, 1793.

[79] C. Harnagea, M. Alexe, J. Schilling, J. Choi, R. B. Wehrspohn, D. Hesse, U. Gösele, *Appl. Phys. Lett.* **2003**, *83*, 1827.

[80] V. A. Shchukin, D. Bimberg, *Rev. Mod. Phys.* **1999**, *71*, 1125.

[81] M. Dawber, I. Szafraniak, M. Alexe, J. F. Scott, *J. Phys. Condens. Matter* **2003**, *15*, L667.

[82] I. Szafraniak, D. Hesse, M. Alexe, in *Handbook of Advanced Dielectric, Piezoelectric and Ferroelectric Materials: Synthesis, Properties and Applications*, (Ed: Z.-G. Ye,), Woodhead Publishing Ltd, Cambridge, UK **2008**, Ch. 20.

[83] a) W. Ma, D. Hesse, *Appl. Phys. Lett.* **2004**, *84*, 2871. b) W. Ma, D. Hesse, *Appl. Phys. Lett.* **2004**, *85*, 3214.

[84] W. Ma, D. Hesse, U. Gösele, *Small* **2005**, *1*, 837.

[85] W. Ma, D. Hesse, U. Gösele, *Nanotechnology* **2006**, *17*, 2536.

[86] W. Lee, M. Alexe, K. Nielsch, U. Gösele, *Chem. Mater.* **2005**, *17*, 3325.

[87] S. K. Lee, W. Lee, M. Alexe, K. Nielsch, D. Hesse, U. Gösele, *Appl. Phys. Lett.* **2005**, *86*, 152906.

[88] J. Choi, K. Nielsch, M. Reiche, R. B. Wehrspohn, U. Gösele, *J. Vac. Sci. Technol. B* **2003**, *21*, 763.

[89] S. K. Lee, D. Hesse, M. Alexe, W. Lee, K. Nielsch, U. Gösele, *J. Appl. Phys.* **2005**, *98*, 124302.

[90] W. Lee, H. Han, A. Lotnyk, M. A. Schubert, S. Senz, M. Alexe, D. Hesse, S. Baik, U. Gösele, *Nat. Nanotechnol.* **2008**, *3*, 402.

[91] H. Zheng, J. Wang, S. E. Lofland, Z. Ma, L. Mohaddes-Ardabili, T. Zhao, L. Salamanca-Riba, S. R. Shinde, S. B. Ogale, F. Bai, D. Viehland, Y. Jia, D. G. Schlom, M. Wuttig, A. Roytburd, R. Ramesh, *Science* **2004**, *303*, 661.

[92] J. Slutsker, I. Levin, J. H. Li, A. Artemev, A. L. Roytburd, *Phys. Rev. B* **2006**, *73*, 184127.

[93] Q. Zhan, R. Yu, S. P. Crane, H. Zheng, *Appl. Phys. Lett.* **2006**, *89*, 172902.

[94] H. Zheng, Q. Zhan, F. Zavaliche, M. Sherburne, F. Straub, M. P. Cruz, L.-Q. Chen, U. Dahmen, R. Ramesh, *Nano Lett.* **2006**, *6*, 1401.

[95] F. Zavaliche, H. Zheng, L. Mohaddes-Ardabili, S. Y. Yang, Q. Zhan, P. Shafer, E. Reilly, R. Chopdekar, Y. Jia, P. Wright, D. G. Schlom, Y. Suzuki, R. Ramesh, *Nano Lett.* **2005**, *5*, 1793.

[96] F. Zavaliche, T. Zhao, H. Zheng, F. Straub, M. P. Cruz, P.-L. Yang, D. Hao, R. Ramesh, *Nano Lett.* **2007**, *7*, 1586.

[97] M. Ziese, A. Setzer, I. Vrejoiu, B. I. Birajdar, B. J. Rodriguez, D. Hesse, *J. Appl. Phys.* **2008**, *104*, 063908.